Chemistry–A European Journal
Full Paper
doi.org/10.1002/chem.202102163
Chemistry Europe
European Chemical Societies Publishing

How Aromatic Fluorination Exchanges the Interaction Role of Pyridine with Carbonyl Compounds: The Formaldehyde Adduct

Juan Carlos López,*[a] Alberto Macario,[a] Assimo Maris,[b] Ibon Alkorta,[c] and Susana Blanco*[a]

Abstract: The rotational spectrum of the weakly bound complex pentafluoropyridine···formaldehyde has been investigated using Fourier transform microwave spectroscopy. From the analysis of the rotational parameters of the parent species and of the ^{13}C and ^{15}N isotopologues, the structural arrangement of the adduct has been unambiguously established. The full ring fluorination of pyridine has a dramatic effect on its binding properties: It alters the electron density distribution at the π-cloud of pyridine creating a π-hole and changing its electron donor-acceptor capabilities. In the complex, formaldehyde lies above the aromatic ring with one of the oxygen lone pairs, as conventionally envisaged, pointing toward its centre. This lone pair···π-hole interaction, reinforced by a weak C–H···N interaction, indicates an exchange of the electron-acceptor roles of both molecules when compared to the pyridine···formaldehyde adduct. Tunnelling doublets due to the internal rotation of formaldehyde have also been observed and analysed leading to a discussion on the competition between lone pair···π-hole and π···π stacking interactions.

Introduction

Non-covalent interactions involving aromatic rings play a pivotal role in chemistry and biology processes such as drug-receptor and protein-ligand recognition interactions or protein folding.[1,2] The aromatic π-cloud acts, in general, as Lewis base in non-covalent interactions. Thus, it is involved in the chelation of cations,[3] and as a hydrogen bond acceptor in biological systems.[1] The substitution of hydrogen atoms by halogens, specifically fluorine atoms, changes the chemical properties of halide molecules enhancing the role of new types of intermolecular non-covalent interactions. These effects have been exploited to tune the properties of drugs[4] and new materials.[5] In aromatic rings, the strong fluorine inductive effect withdraws the electron density of the π-cloud region that may become electron-deficient. This region, often recognized as a π-hole,[6] now acts as Lewis acid[7–10] that can interact with lone-pair bearing atoms and would enhance anion-π interactions.[9,11] These lone pair···π interactions have been identified in protein[12,13] and solid-state structures.[14] Studies on isolated model adducts of hexafluorobenzene···water (C_6F_6···H_2O),[15,16] pentafluoropyridine···water (C_5F_5N···H_2O)[17] or the related complexes with ammonia (C_6F_6···NH_3 and C_5F_5N···NH_3)[18] have unambiguously proved the interaction between the oxygen or nitrogen lone pairs and the electron-deficient π-clouds of the fully fluorinated aromatic rings. It should be noted that in these cases, the complexes with the corresponding non-fluorinated rings are stabilized by hydrogen bond interactions.[19–23]

The interaction between carbonyl groups and aromatic moieties has been observed in protein structures between C=O amide groups and aromatic residues with geometries that lie between those of an ideal π···π and ideal lone pair···π interaction.[13] However, there are no studies on model adducts giving experimental evidence on the interactions of the lone pairs of a carbonyl group with a π-hole created by fluorination on an aromatic ring. In this paper, we present a rotational study of the adduct between pentafluoropyridine and formaldehyde (C_5F_5N···H_2CO) as a model of the interaction of the carbonyl group with perfluoro azines. Of additional interest is the fact that the dominant interaction in the complexes of pyridine with carbonylcompounds[24,25] is an $n\rightarrow\pi^*$ interaction which involves the delocalization of the lone pair (n) of pyridine N atom into the antibonding (π^*) orbital of the acceptor carbonyl group. Until now there is no experimental evidence about the possible competition between the lone pair···π-hole and the $n\rightarrow\pi^*$ interactions. We show how the presence of the fluorine atoms changes the electron donor-acceptor roles of both molecules when compared to those observed in the pyridine···H_2CO adduct.[24]

[a] Prof. J. C. López, Dr. A. Macario, Prof. S. Blanco
Departamento de Química Física y Química Inorgánica
Facultad de Ciencias, IU CINQUIMA
Universidad de Valladolid, 47011 Valladolid (Spain)
E-mail: juancarlos.lopeza@uva.es
susana.blanco@uva.es

[b] Prof. A. Maris
Dipartimento di Chimica "G. Ciamician"
Università di Bologna
Via Selmi 2, I-40126 Bologna (Italy)

[c] Prof. I. Alkorta
Instituto de Química Médica (CSIC)
Juan de la Cierva 3, 28006 Madrid (Spain)

Supporting information for this article is available on the WWW under https://doi.org/10.1002/chem.202102163

Fourier transform microwave (FTMW) spectroscopy in combination with supersonic-jet techniques[26–28] is particularly suited to study weakly bound molecular complexes, allowing to explore their structure, intermolecular interactions, and dynamics.[24,29,30] The structural data obtained from this technique have shown the fundamental differences between interactions like the C–H···π bond in benzene···H_2O[19,20] or corannulene···H_2O[31] and the lone pair···π-hole contact responsible for the formation of C_6F_6···H_2O.[16] In the same way, one could compare the differences between the O–H···N hydrogen bond, forming pyridine···H_2O,[21] the lone pair···π-hole contact observed in C_5F_5N···H_2O[17] or the $n\rightarrow\pi^*$ interaction dominating the pyridine···H_2CO adduct.[24] Furthermore, the rotational spectrum shows the rich intermolecular dynamics associated with the internal rotation and other intermolecular vibrations of the adduct, ranging from free rotation in C_6F_6···H_2O[16] or corannulene···H_2O[31] to hindered rotations as occur in pyridine···H_2O[21] or triacetonetriperoxyde···H_2O.[30]

Results and Discussion

Before searching the possible conformations of the complex C_5F_5N···CH_2O, the molecular electrostatic potential (MESP) for the isolated monomers was analyzed in order to locate those regions with positive and negative values that could interact with electron-rich and poor regions of other systems, respectively. The MESPs on the 0.001 au electron density isosurface calculated at the CCSD/6-311++G(2d,p) computational level are shown in Figure 1. Positive regions in C_5F_5N are found above and below the aromatic ring with the largest values between the *para* and *meta* fluorine atoms (0.042 au) followed by the region above/below the center of the ring (0.040 au) and the region between the *ortho* and *meta* fluorine atoms (0.036 au). All the periphery of the system shows negative values, associated with the fluorine atoms ranging between −0.003 and −0.017 au. The most negative region is the one associated with the lone pair to the nitrogen atom (−0.032 au). Those regions have their complementarities in the H_2CO subunit, a positive region around the C–H bonds with the maximum value (0.048 au) just between them, and a negative region around the oxygen atom being the most negative values (−0.048 au) coincident with the lone pair domains.

A search of the possible conformers of C_5F_5N···H_2CO was done using CREST[32] and following chemical intuition based on the MESP (see Figure 1) to explore the different docking sites. To have reasonable starting parameters to explore the rotational spectrum, structure optimizations of the initial forms were then done using G16 package[33] at MP2/6-311++G(2d,p) level,[34,35] usually giving good predictions of the quadrupole coupling parameters.[29] In addition, density functional theory (DFT) optimizations were done using B3LYP hybrid functional[36] with the same basis set and including D3[37] and D3BJ[38] empirical dispersion corrections. Eight stationary points in the potential energy surface (PES) were obtained (See Figure S1). Harmonic frequency MP2 calculations predict all the forms to be local minima, whereas DFT computations only predict C1 and C3 as minima in the PES, the rest being predicted as first-order saddle points. The three most stable forms, C1, C2, and C3, shown in Figure 2, have H_2CO lying above the ring plane. In the C1 global minimum, with C_s symmetry, H_2CO lies on the symmetry plane perpendicular to the C_5F_5N ring. The oxygen atom points to the ring centroid suggesting the formation of a π-hole interaction. The H_2CO hydrogen atom closest to the ring is pointing to the nitrogen atom establishing a weak C–H···N hydrogen bond. By considering the MESP shown in Figure 1, in the C1 structure the negative region of H_2CO associated with the lone pairs of the oxygen interacts with the positive regions in the center of the aromatic ring of C_5F_5N, and the positive region of one of the CH groups of H_2CO contacts with the lone pair of the nitrogen of C_5F_5N. Similar contacts support form C3 where the negative region of H_2CO interacts with the positive region between the *para* and *meta* fluorine atoms while a C–H group interacts bifurcately with the *meta* and *para* fluorine atoms.

Configuration C2 is related to form C1 through the rotation of H_2CO by 90° around its local C_2 axis. The potential energy profile from relaxed scans on this rotation of H_2CO predicts configuration C2 as a shallow minimum at MP2 level and as a saddle from DFT calculations as is shown in Figure 3. In C4-C8 forms, H_2CO lies in the ring plane showing different C–H···N, C–H···F weak hydrogen bond or C–F···O halogen bond interactions. All these forms, whose relative energy is between 15 and 20 kJ/mol with respect to the global minimum, are predicted as saddle points with one imaginary frequency

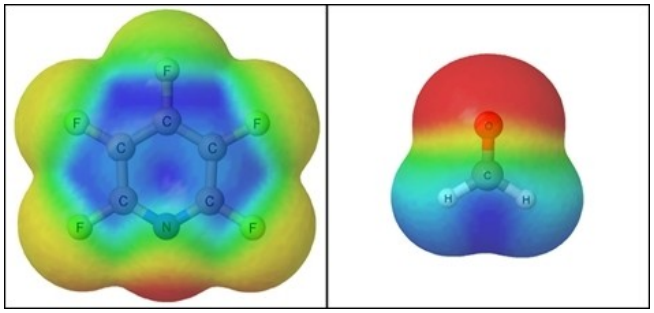

Figure 1. Molecular electrostatic potential on the 0.001 au electron density isosurface for the isolated monomers (CCSD/6-311++G(2d,p)). The values are represented between > +0.04 au (blue) and < −0.025 au (red).

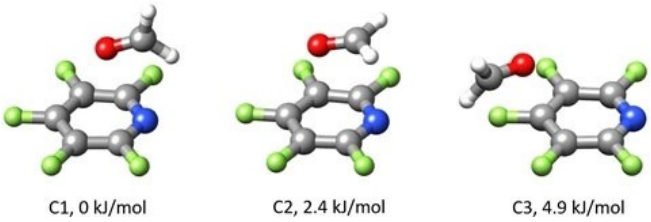

Figure 2. Conformers of the C_5F_5N···H_2CO adduct calculated as minima at MP2/6-311++G(2d,p) and their relative energies. The conformers have been labelled C1, C2, C3, in order of increasing energy. C2 is calculated to be a saddle point using other methods (see text).

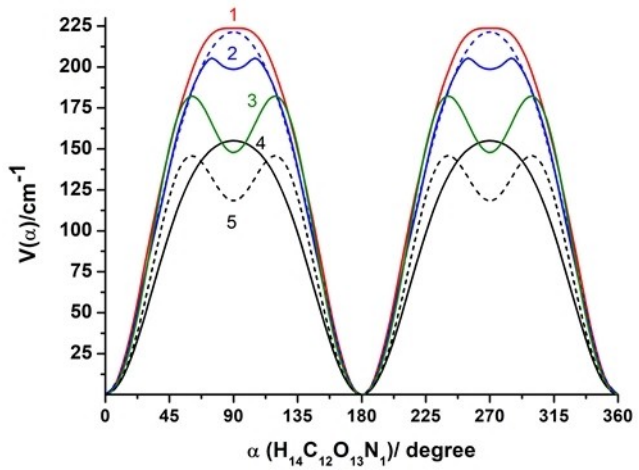

Figure 3. Potential energy function for the rotation of H_2CO around its local C_2 axis for the adduct $C_5F_5N\cdots H_2CO$. The minima at 0° and 180° correspond to conformer C1 and the points at 90° and 270° correspond to structure C2. The profile has been calculated at (1) B3LYP-D3BJ/6-311++G(2d,p); (2) MP2/ 6-311++G(2d,p), dashed line constraining the C=O bond to lie in the σ_{bc} symmetry plane; (3) MP2/aug-cc-pVTZ; (4) Function $V(\alpha) = 155(1-cos(2\alpha))/2 + 21(1-cos(4\alpha))/2$ cm^{-1} reproducing experimental data according to flexible model calculations; (5) Function $V(\alpha) = 132.8(1-cos(2\alpha))/2 + 32.7(1-cos(4\alpha))/2 - 14.4(1-cos(6\alpha))/2$ cm^{-1} reproducing experimental data according to flexible model calculations.

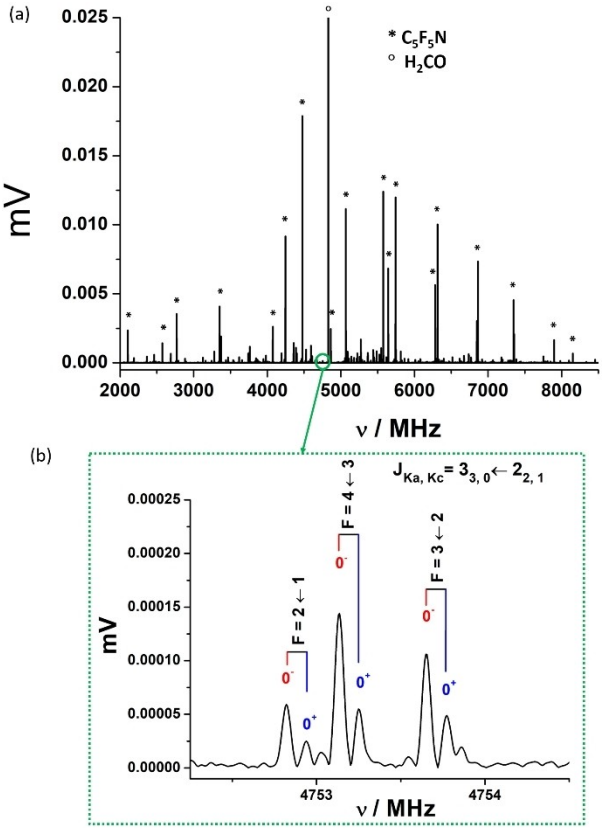

Figure 4. (a) Observed broadband FTMW spectrum (2-8 GHz) dominated by the spectra of C_5F_5N (*) and CH_2CO (°). (b) The $3_{3,0}\leftarrow 2_{2,1}$ transition assigned to the parent species of $C_5F_5N\cdots H_2CO$ showing the $F+1\leftarrow F$ quadrupole coupling hyperfine components and the $0^+/0^-$ doublets with an intensity ratio close to 1/3.

related to out of plane motions by DFT calculations. Consequently, as occur for C2, the forms C4-C8 calculated at MP2/6-311++G(2d,p) level may correspond to shallow minima located at saddle point regions of the PES, connecting the equivalent conformers of C1 or C3 forms with H_2CO above or below the C_5F_5N ring plane. For structures C1, C2, and C3 further optimizations were run using MP2 method with aug-cc-pVDZ and aug-cc-pVTZ basis sets.[39] At these levels, both MP2 calculation predict C2 to be a saddle point with respect to the bending motion of the two planar moieties with respect to the symmetry plane. The MP2/aug-cc-pVTZ potential energy profile on the rotation of H_2CO relating C1 and C2 forms is also shown in Figure 3. Finally we optimized C1 and C2 using the CCSD/6-311++G(2d,p) computational level.[40] The rotational constants and electric dipole moment components calculated for C1-C3 forms at the different levels are given in Tables S1-S6.

The broadband FTMW spectrum of $C_5F_5N\cdots H_2CO$ was recorded in the 2–8 GHz region using a chirped-pulse Fourier transform microwave spectrometer[41] described elsewhere.[42] Further measurements of the $C_5F_5N\cdots H_2CO$ spectrum were done in the 6–12 GHz range using a narrowband Balle-Flygare Fourier transform spectrometer[43] with a coaxial orientation of the molecular beam and the axis of the Fabry-Perot resonator.[44] The broadband spectrum (Figure 4) is dominated by strong signals from the H_2CO[45] and C_5F_5N[46] monomers and less intense transitions from the $C_5F_5N\cdots H_2O$[17] adduct already studied. The spectra of the ^{13}C and ^{15}N species of C_5F_5N in their natural abundance were also easily observed and measured together with the parent species lines. A detailed exploration of the spectrum based on the theoretical predictions done on $C_5F_5N\cdots H_2CO$ lead to the assignment of the rotational lines of a weak species showing only a μ_b-type spectrum identifiable as the C1 form of $C_5F_5N\cdots H_2CO$. As can be seen in Figure 4b, all the transitions of this rotamer show the quadrupole coupling hyperfine structure (hfs) due to the presence in C_5F_5N of a ^{14}N nucleus with patterns comparable to those predicted for conformer C1. Each hfs component consists of closely spaced doublets labeled 0^+ and 0^- with lines showing an intensity ratio of ca. 1/3. We have seen (see Figure 3) that the internal rotation of H_2CO around its local symmetry axis in the $C_5F_5N\cdots H_2CO$ adduct is governed by a periodic potential energy function which passes successively through geometries C1 and C2. The small barrier at C2 form is high enough to split the vibrational states below the barrier in tunneling doublets. Such a motion would exchange the two hydrogen atoms of H_2CO, a pair of fermions ($I = {}^1/_2$), giving, as a result, a 1/3 nuclear spin statistical weight effect which is reflected in the intensities observed in the rotational spectrum. Similar doublets were observed in the rotational spectrum of $C_5F_5N\cdots H_2O$[17] that were proved to correspond to the rotation of water around its C_2 axis. Further support on the identification of this conformer comes from the measurements using the narrow-band spectrometer (see Figure S2). The sensitivity of this instrument allowed us to measure

all ^{13}C and ^{15}N isotopologues of $C_5F_5N\cdots H_2CO$ in their natural abundances.

The analysis[47] of the measured spectra was done using a Hamiltonian including semirigid rotor and quadrupole coupling[48] terms. The semirigid rotor Hamiltonian was set up in the A-reduction of Watson[49] and I^r representation. The tunneling states could be treated independently but in the final fit, they were fitted together using a two-states Hamiltonian to constrain the centrifugal distortion and quadrupole coupling constants to have the same values in both states. The spectra of all isotopologues were fitted by keeping the centrifugal distortion and quadrupole coupling constants fixed to the parent species values. The results of the analysis of the parent species of C_5F_5N and $C_5F_5N\cdots H_2CO$ are given in Table 1 where they are compared to the best theoretical predictions. The spectroscopic constants of the monomer C_5F_5N are more accurate than those determined previously[46] being a valuable benchmark for the theoretical calculations (see Table S7). All methods except for MP2/aug-cc-pVDZ give values of the C_5F_5N rotational constants close to the experimental values, the MP2/aug-cc-pVTZ calculations giving the most accurate results. The same degree of agreement is obtained only at the CCSD/6-311++G(2d,p) level for $C_5F_5N\cdots H_2CO$ (see Table S9). The quadrupole coupling constants are very well reproduced at MP2/6-311++G(2d,p) level for both the monomer and the cluster (Tables S7 and S9) as has been previously observed.[29] The rotational parameters and the frequencies measured for all the species are given in the Supporting Information (Tables S17–S27).

The comparison of the spectroscopic parameters of the monomer C_5F_5N and the cluster $C_5F_5N\cdots H_2CO$ provides fine insights into the structure of the complex, information not dependent on the theoretical calculations. C_5F_5N and H_2CO are planar molecules with C_{2v} symmetry (see Table S11), the σ_{ab} inertial plane being the molecular plane. The plane of these molecules is thus a symmetry plane coincident in both cases with the σ_{ab} inertial plane. The planar moment P_{cc} value giving the mass extension out of the *ab* inertial plane is nearly zero in both cases (see Table S11 and Figure 5, where the principal axes of C_5F_5N are labelled with a prime). Otherwise, P_{cc} is rather large in the case of the cluster (about 207.98 uÅ^2, see Table 1), indicating that H_2CO lies above or below the C_5F_5N ring plane. The C_2 axis of C_5F_5N is the *b* inertial axis and the symmetry plane perpendicular to the molecule corresponds to the σ_{bc} inertial plane. The planar moment P_{aa}, giving the mass extension out of the *bc* plane is nearly the same for the monomer and the cluster (see Table 1). This proves that the H_2CO molecular plane (σ_{ab}) is coincident with the σ_{bc} plane of C_5F_5N consistently with a C_s symmetry of $C_5F_5N\cdots H_2CO$ as occurs for conformer C1. The coincidence of the σ_{bc} planes of the C_5F_5N monomer and the $C_5F_5N\cdots H_2CO$ adduct is confirmed by the nearly equal values P_{aa} for the parent, ^{15}N isotopologues, and all those ^{13}C atoms lying on the σ_{bc} inertial plane of the monomer and cluster (see tables S8 and S10).

The spectroscopic constants associated with quadrupole coupling terms, $\chi_{\alpha\beta}$ ($\alpha,\beta = a, b, c$), are related to the coupling of the ^{14}N nuclear quadrupole moment ($I = 1$), eQ, with the electric field gradient, q, created by the rest of the molecular charges at N nucleus.[48] These constants are practically a direct measure of the electric field gradient tensor elements at the nitrogen nuclei ($\chi_{\alpha\beta} = eQq_{\alpha\beta}$). The quadrupole coupling tensor of C_5F_5N is diagonal in the principal inertial axis system representation, thus this axis system is coincident with the principal quadrupole coupling axis system (i.e. $a\rightarrow y$, $b\rightarrow z$, $c\rightarrow x$).[46] The preservation

Table 1. Rotational parameters obtained from the semirigid rotor analysis of C_5F_5N and the 0^+ and 0^- torsion states of the $C_5F_5N\cdots H_2CO$ adduct. The experimental parameters of the monomer are compared with those from MP2/aug-cc-pVTZ (MP2) predictions. For the adduct, the parameters are compared to the CCSD/6-311++G(2d,p) (CCSD) results.

Parameters[a]	C_5F_5N		C_5F_5N-H_2CO		
	Exp.	MP2[c]	0^+	0^-	CCSD[d]
A [MHz]	1481.58184(19)[b]	1481.2	779.69465(13)	779.69184(13)	783.9
B [MHz]	1075.37335(17)	1074.2	745.85829(10)	745.82527(10)	748.0
C [MHz]	623.11194(16)	622.7	555.481998(67)	555.464049(67)	556.5
P_{aa} [uÅ^2]	469.95288(16)	470.5	469.60388(15)	469.63241(15)	469.5
P_{bb} [uÅ^2]	341.10379(16)	341.2	440.19896(15)	440.19983(15)	438.6
P_{cc} [uÅ2]	0.00399(16)	0.0	207.97671(15)	207.97818(15)	206.1
Δ_J [kHz]	0.0290(30)		0.2013(11)		
Δ_{JK} [kHz]	[0.0]		1.1527(70)		
Δ_K [kHz]	0.0565(24)		−1.1305(73)		
δ_J [kHz]	0.00474(47)		0.02584(63)		
δ_K [kHz]	0.0343(18)		0.2491(37)		
1.5(χ_{aa}) [MHz]	2.9496(31)	2.76	2.9597(28)		3.12
0.25(χ_{bb}-χ_{cc}) [MHz]	−1.48514(91)	−1.46	−0.76025(79)		>M->0.84
χ_{aa} [MHz]	1.9664(53)	1.84	1.9731(19)		2.08
χ_{bb} [MHz]	−3.9534(72)	−3.83	−2.5071(25)		−2.71
χ_{cc} [MHz]	1.9870(72)	1.99	0.5339(25)		0.63
n	366		237		
σ [kHz]	5.8		3.5		

[a] *A*, *B*, and *C* are the rotational constants. Δ_J, Δ_{JK}, Δ_K, δ_J, and δ_K are the quartic centrifugal distortion constants. χ_{aa}, χ_{bb}, and χ_{cc} are the ^{14}N nuclear quadrupole coupling constants. *n* is the number of hyperfine quadrupole components fitted. σ is the rms deviation of the fit. $P_{\alpha\alpha}$ ($\alpha = a$, *b* or *c*) are the planar moments of inertia derived from the moments of inertia I_α for example $P_{cc} = (I_a + I_b - I_c)/2$. [b] Standard errors are given in parentheses in units of the last digits. [c] MP2/aug-cc-pVTZ is the method that better reproduces the C_5F_5N rotational constants (see Table S7). [d] CCSD/6-311++G(2d,p) is the method that better reproduces the $C_5F_5N\cdots H_2CO$ rotational constants (see Table S9).

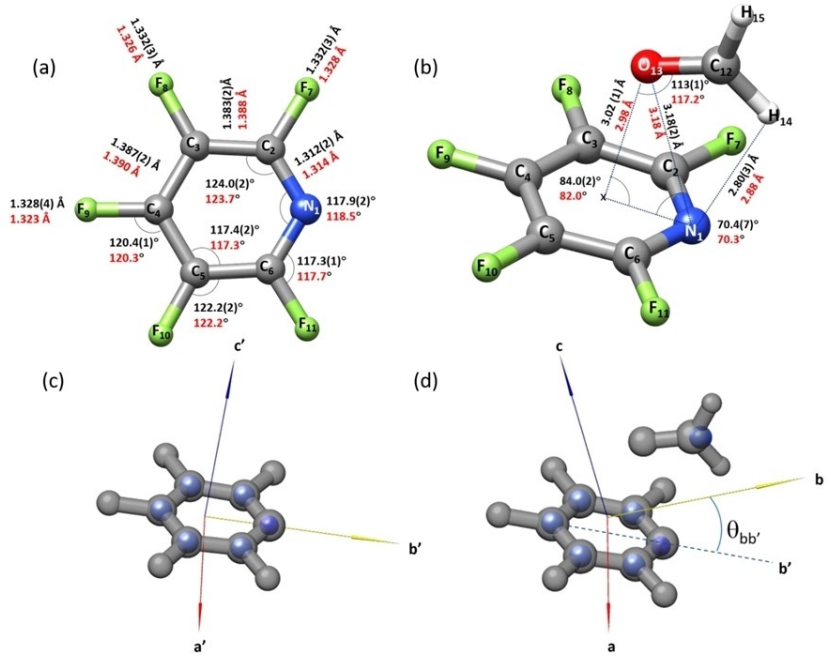

Figure 5. (a) Comparison of the r_0 and r_e (MP2/aug-cc-pVTZ, red) structures of C_5F_5N. (b) Comparison of the r_0 and r_e (CCSD/6-311++G(2d,p), red) structures of the $C_5F_5N\cdots CH_2CO$ adduct. (c) and (d) compare the same r_e structure with the r_s location of the carbon and nitrogen atoms. The inertial axes of the C_5F_5N monomer are labelled as *a*′, *b*′, *c*′, and those of the adduct as *a*, *b*, *c*. Upon complexation, the symmetry plane perpendicular to the C_5F_5N ($\sigma_{b'c'}=\sigma_{bc}$) is preserved so that the orientation of the *a*′ and *a* axes is also preserved. The angle $\theta_{bb'}$ thus defines the rotation around the *a* axis to bring the orientation of *b*′ and *c*′ axes of the monomer into that of *b* and *c* axis in the complex.

of the σ_{bc} plane as a symmetry plane in the complex implies that the orientation of the *a/y* inertial/quadrupole coupling axis is also preserved in the complex as can be deduced from the fact that the χ_{aa} quadrupole coupling constant has nearly the same values in C_5F_5N and the adduct $C_5F_5N\cdots H_2CO$ (see Table 1). For the same reason, the orientation of the *b* and *c* inertial axes of the cluster results from the rotation of the monomer axes by an angle $\theta_{bb'}$ as defined in Figure 5. Using a value of $\theta_{bb'}=29.6°$ to transform the experimental quadrupole coupling tensor constants of the monomer into those expected for the adduct it gives $\chi_{bb}=-2.504$ MHz and $\chi_{cc}=0.538$ MHz, values very close to the experimental values for $C_5F_5N\cdots H_2CO$ (see Table 1). This evidences that the electric field gradient and thus the electronic environment around N atom is not altered upon formation of the complex.

The structures of both C_5F_5N and $C_5F_5N\cdots H_2CO$ have been finally investigated from the analysis of the rotational parameters of all measured isotopologues using the r_s and r_0 methods. In the case of the adduct, the arithmetic mean of the parameters obtained for both tunneling states was used. The substitution, r_s, structure corresponds to the set of coordinates of all isotopically monosubstituted atoms relative to the principal inertial axis system of the parent molecule. The comparison of the inertial moments of the parent and monosubstituted isotopologues through the Kraitchman equations[50] leads to the absolute values of the substituted atom coordinates. The signs of the coordinates can be assigned from any reasonable geometry like effective (r_0) or theoretical (r_e) structures. This experimental approach has some limitations in locating atoms close to the principal inertial axes or for light atoms like hydrogen. A total or partial effective r_0 structure can be obtained when bond distances and angles are obtained from a least-squares fit of the inertial moments of all observed isotopologues.[51]

Giving the good agreement between the experimental and MP2/aug-cc-pVTZ rotational constants the ab initio structure calculated at this level of theory was chosen as starting point in the r_0 fittings for C_5F_5N. The only constraints were to keep a C_{2v} symmetry, setting equal C–F distances for the F_7, F_8, F_{10}, and F_{11} atoms (see Figure 5 for atom labeling). Additionally, the FCC angles were fixed to the theoretical predictions. This experimental structure (see Figure 5) and the r_0 H_2CO structure, corrected with the small changes predicted by ab initio calculations on the formation of the $C_5F_5N\cdots H_2CO$ complex, were kept fixed in the r_0 fit to determine the $C_5F_5N\cdots H_2CO$ intermolecular bond distances and angles. The determined r_s and r_0 structures of C_5F_5N and $C_5F_5N\cdots H_2CO$ are given in Tables S12-S15 and summarized in Figure 5, where they are compared with the theoretical results. While the C_5F_5N experimental structure is reasonably well reproduced by theoretical calculations, the structure of the heterodimer shows evident discrepancies between experiment and DFT or MP2 predictions which could be associated with the difficulties to describe the balance of weak interactions responsible for its formation. However, the experimental structure of the dimer is reproduced to a reasonable agreement by the CCSD/6-311++G(2d,p) calculations as observed in other complexes formed by weak

interactions as pyridine···formaldehyde (C_5H_5N···H_2CO)[24] or pyridine···acetaldehyde (C_5H_5N···CH_3CHO).[25]

The shape of the potential energy function associated with the torsional dihedral angle coordinate α ($\angle H_{14}C_{12}O_{13}N_1$) (see Figure 5 for labeling) describing the internal rotation of H_2CO around its C_2 local symmetry axis was explored at MP2/6-311++G(2d,p), MP2/aug-cc-pVTZ, and B3LYP-D3BJ/6-311++G(2d,p) levels as can be seen in Figure 3. In the MP2/6-311++G(2d,p) exploration, no restrictions were imposed and the PES gives the shape shown in Figure 3 (continuous blue trace 2) with minima at 0° and 90° corresponding to forms C1 and C2, respectively. Unfortunately, given the flat nature of the PES near to the C2 form, which is also apparent from the DFT calculations (Figure 3, red trace 1), the calculated intermolecular parameters do not strictly follow a continuous variation for values of α between 60° and 120°. For this reason, in a second MP2/6-311++G(2d,p) exploration, the C=O bond was constrained to lie in the σ_{bc} plane of C_5F_5N while all the other parameters were freely optimized. A double minimum PES (Figure 3, dashed blue trace 2) was obtained. In this case, the intermolecular parameters follow a continuous variation with the same trends as those in the scan with no constraints below $\alpha > 60°$ and not very different from those calculated at the B3LYP-D3BJ/6-311++G(2d,p) level. Repeating the constrained procedure at MP2/aug-cc-pVTZ level a PES showing minima at both C1 and C2 configurations is obtained (Figure 3, green trace 3). However, this C2 structure with C_s symmetry is not a real minimum but a saddle point for a bending motion of the H_2CO with respect to the symmetry plane. It is worth noting that at the CCSD/6-311++G(2d,p) level the predicted geometry for C2 configuration is rather different than those calculated from DFT or MP2 methods as is shown in Figure S3.

Starting from the last set of results, Meyer's flexible model[52] was used to deduce the potential energy function of the motion. The potential and structural relaxation parameters were adjusted to reproduce the differences of the experimental planar moments of inertia ΔP_{aa}, ΔP_{bb}, and ΔP_{cc} between the two observed states (0^+ and 0^-). As detailed in the Supporting Information, we have tested both types of potential energy functions describing the H_2CO torsion pathway, the periodic two-fold double minimum function:

$$V(\alpha) = V_2(1 - cos(2\alpha))/2 + V_4(1 - cos(4\alpha))/2 \quad (1)$$

where V_2 gives the two-fold barrier size while V_4 shapes its width and the periodic function with minima at C1 and C2:

$$V(\alpha) = V_2(1 - cos(2\alpha))/2 + V_4(1 - cos(4\alpha))/2 + V_6(1 - cos(6\alpha))/2 \quad (2)$$

where the α values of 0°, 180°, and 360° correspond to the equilibrium configuration C1 with H_2CO lying in the σ_{bc} plane perpendicular to the ring and containing the nitrogen atom (see Figure 5). A negative value of V_6 in Equation (2) leads to additional minima at 90° and 270° for the C2 configuration. Both (1) and (2) potential energy functions would predict the lowest energy torsional states as a doublet with a small energy difference as was experimentally observed.

Theoretical calculations indicated that the intermolecular parameters undergo a considerable structural relaxation upon the internal rotation of formaldehyde. We have considered the variation of the $r(C_{12}N_1)$ distance and the $\angle C_{12}N_1C_4$ and $\angle O_{13}C_{12}N_1$ angles (see Figure 5 for labeling) to better reproduce the experimental results. Using Equation (1) the experimental values of the planar moments are reproduced to a reasonable agreement ($\Delta P_{aa} = 0.028$ uÅ^2, $\Delta P_{bb} = -0.001$ uÅ^2, and $\Delta P_{cc} = 0.001$ uÅ^2) for the potential energy function shown in Figure 3 (black continuous, trace 4) with $V_2 = 155$ cm^{-1} and $V_4 = 21$ cm^{-1}. When using the potential function of Equation (2) the same degree of agreement between experimental and calculated parameters was obtained for values of the potential energy parameters $V_2 = 132.8$ cm^{-1}, $V_4 = 32.7$ cm^{-1}, and $V_6 = -14.4$ cm^{-1} (Figure 3, black dashed, trace 5). This function predicts that the C2 structure is 118.4 cm^{-1} higher in energy than C1 with interconversion barriers of 145.8 cm^{-1}. The C2 energy calculated at CCSD/6-311++G(2d,p) (138 cm^{-1}) lies between the C2 energy values estimated for potential function (1) of 155.0 cm^{-1} and that of function (2) of 118.0 cm^{-1}. The fact that both potential energy functions describe the experimental observations is not a surprise since the observed rotational constants reflect the energy profile and torsion dynamics near the C1 minimum and this is described practically in the same way in both models.

To get more insight into the nature of the intermolecular interactions responsible for the formation of the complex we have deeply analyzed the theoretical data. The interaction between the two molecules has been studied using the electron density by means of the quantum theory of "atoms in molecules" (QTAIM)[53] and noncovalent interaction plot (NCIPlot)[54] analysis (see Figure 6). The QTAIM shows the presence of two intermolecular bond critical points (BCPs). One of them is found following the bond path (BP) describing a weak C–H···N contact associated with the electrostatic interaction previously mentioned. The other BCP is at the BP connecting the O and N atoms in some way describing an O···N weak bond. The characteristics of the electron density at the intermolecular BCPs (small values of the electron density, 0.008

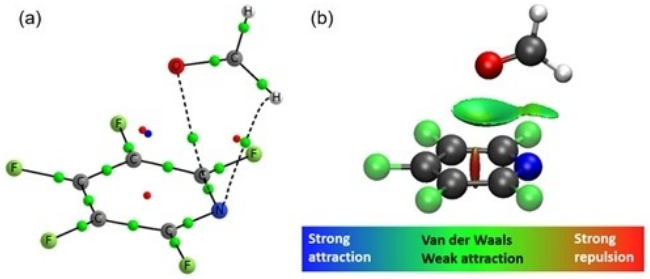

Figure 6. (a) Molecular graph of the most stable complex form (C1) using the CCSD/6-311++G(2d,p) wave function. The green, red and blue dots represent the location of the bond, ring, and cage critical points. (b) 3D-NCIPlot isosurface at s = 0.5 coloured according of sign(λ_2)ρ, ranging from −0.03 to 0.03 au.

and 0.005 au, respectively, and positive values of the Laplacian) denote that they correspond to weak interactions. The isolated ring and cage critical points are a consequence of the electron density in this region. The two 2D contour plots shown in Figure S4 provide clues on how the electron density changes around these critical points. In addition, the proximity of both critical points is an indication that the topological description is close to a catastrophic point.

The NCIPlot of the complex shows two clouds with green color, as an indication of weak interactions, corresponding to the same contacts. As a difference with the QTAIM results, the electrostatic interaction between the carbonyl oxygen and the C_5F_5N ring, or in other words the lone pair···π-hole interaction, is evident from the NCIPlot results. NBO calculations at DFT level show a stabilization due to the electron transfer from the lone pair of the oxygen towards the antibonding orbitals of C_5F_5N that accounts for 1.75 kJ/mol stabilization. In the same way, the charge transfer from the nitrogen lone pair towards the antibonding CH is associated with 1.63 kJ/mol stabilization energy. The energy decomposition analysis of the most stable conformer with the DFT-SAPT[55,56] method shows that the electrostatic and dispersion terms contribute almost equally to the stabilization of the complex (−17.1 and −16.8 kJ/mol, respectively) while the induction term does not show a significant contribution (−2.0 kJ/mol). These terms are partially compensated by the repulsive exchange term (+19.6 kJ/mol). These values are comparable to those obtained for complexes of C_6F_6 or C_5F_5N with water,[18] and C_5H_5N with CH_2O (see Table S16).

It is interesting to compare the structure of $C_5F_5N\cdots CH_2O$ with those of related complexes. In $C_5H_5N\cdots CH_2O$[24] all the heavy atoms are in the ring plane reflecting the fact that the main contact is an N···CO n→π* interaction involving the delocalization of the pyridine N lone pair into the antibonding π* orbital of CH_2O. This is further stabilized by a weak C–H···O hydrogen bond. In contrast, in the present case, CH_2O lies above the C_5F_5N ring in $C_5F_5N\cdots CH_2O$ reflecting that the main interaction is a lone pair···π contact. The distance from the oxygen atom to the ring centroid (x), 3.02 Å, is comparable to those observed in the $C_6F_6\cdots H_2O$ (3.05 Å)[16] or $C_5F_5N\cdots H_2O$ (3.00 Å)[17] complexes. The same can be said about the *r*(O···N) distances, 3.18 Å in $C_5F_5N\cdots H_2CO$ and 3.16 Å in $C_5F_5N\cdots H_2O$. The angle ∠OxN of 84.0° in $C_5F_5N\cdots H_2CO$ is also comparable to that of 83.8° observed in $C_5F_5N\cdots H_2O$ while in $C_6F_6\cdots H_2O$ the corresponding angle is of 90°. The deviation from the ideal 90° value of the ∠OxN angles in the C_5F_5N complexes are due to the existence of weak C–H···N or O–H···N hydrogen bond contacts contributing to the stability of the global minimum. This C–H···N contact in $C_5F_5N\cdots H_2CO$ is characterized by a short distance *r*(H···N) of 2.80 Å and an angle ∠CH···N of 110.6°, far from the ideal value of 180°. Unfortunately, no N···H data have been reported on this possible interaction for $C_5F_5N\cdots H_2O$. The agreement of these structural data is very good despite the differences in the electronic structures of water and H_2CO.

The structures of the contacts between carbonyl groups and aromatic rings in proteins[13] reveal a wide range of interactions with *r*(O···x) distances that, except for a few cases with values between 2.8 and 3.0 Å, lie in in the range between 3.0 and 3.5 Å (see Figure 1 in Ref. [13]). The angles involving the O atom, the ring centroid and one of the aromatic carbons exhibit a preference for 60–120° values. However, in those cases, the angle between the plane of the ring and the $R_2C{=}O$ group has been used to characterize the contribution of the π···π or lone-pair···π interactions to the contacts. A pure π···π interaction would exhibit a dihedral angle close to zero while a pure lone pair···π interaction would give values close to 90°. The protein structures with aromatic groups coming from residues as histidine, tyrosine, phenylalanine, or tryptophan, give a dihedral angle distribution between 25° and 65° indicating that π···π interactions have an important contribution but that lone-pair···π interactions cannot be ruled out. The structure obtained here for the isolated complex $C_5F_5N\cdots H_2CO$ have distances and angles that lie within the values observed in protein structures. However, the dihedral angle between molecular planes is of 90°, corresponding to a pure lone-pair···π interaction. In this way, the experimental structure reported here for $C_5F_5N\cdots H_2CO$ can be taken as a good model for the interaction between the carbonyl group and an aromatic ring.

Another point of interest is the dynamics of the complex. We have observed the doublets arising from the internal rotation of the H_2CO around its local C_2 axis. This motion is governed by a periodic motion that exchanges the two equivalent forms of the equilibrium global minimum through a barrier centered at a configuration, which we have labeled C2. The barrier around 155.0 cm^{-1}, three times higher than that observed for a similar motion of water in the complex $C_5F_5N\cdots H_2O$,[17] contrasts with the free internal rotation of water in $C_6F_6\cdots H_2O$.[16] These barriers arise from the presence of the nitrogen atom in the ring of C_5F_5N. In the case of $C_5F_5N\cdots H_2CO$ the barrier may confirm the existence of a small C–H···N interaction stronger than in the case of the O–H···N contact for $C_5F_5N\cdots H_2O$. One point open is the shape of the barrier around C2 configuration whether it is maximum or not and the geometry adopted by the complex for it. As shown in Figure S3 the predicted configurations are different at the various levels of calculations. While for DFT and MP2 calculations the predicted configuration seems to be dominated by a π···π interaction between the ring and the carbonyl group, for the CCSD prediction, the structure is likely corresponding to a lone-pair···π interaction. These contributions are reflected in the QTAIM molecular graphs calculated at MP2 and CCSD levels shown in Figure S5. Given the good agreement between the experimental and CCSD rotational constants and the fact that MP2 level tends to overestimate π···π interactions,[57] one could assume that the CCSD C2 structure is more reliable. In such case, the lone-pair···π interaction would be dominant with the extra contribution of the C–H···N weak interaction at the minima.

Conclusion

In this work, we show how the perfluorination of the pyridine ring completely changes the properties of this system. The

interaction of C_5H_5N with carbonyl compounds as H_2CO[24] or acetaldehyde[25] is dominated by a rather strong n→π* interaction with a charge transfer contribution due to the partial delocalization of lone pair of nitrogen into the non-bonding π orbital of the carbonyl group. The most favorable n→π* interaction should correspond to a N–C-O angle around 90°. In structure C4 (see Figure S1) this angle is much larger since one of the F atoms in *ortho* position and the carbonyl oxygen seem to repel each other and tend to separate. Therefore, the perfluorination of the pyridine ring completely changes the electron donor-acceptor roles of both molecules which now interact through lone-pair···π-hole contacts in the two stable forms, C1 and C3, of C_5F_5N···H_2CO. In the observed most stable form, C1, the lone pairs of the carbonyl oxygen interact with the π-hole created at the center of the ring. The low barrier observed for the internal rotation of the formaldehyde moiety allows indeed the tunneling exchange of the interacting lone-pairs and C–H groups. The exchange of the equivalent H atoms is evident from the 1:3 nuclear spin statistical weight effects observed in the tunneling doublets.

Experimental Section

Commercial samples of C_5F_5N and H_2CO were used without further purification. The spectrum of the C_5F_5N···H_2CO complex was investigated using a BrightSpec chirped-pulse Fourier transform microwave spectrometer (CP-FTMW)[41] described elsewhere,[42] and a narrowband Fabry-Perot Fourier transform microwave spectrometer (FP-FTMW).[44,58] A small amount of paraformaldehyde powder was placed in a reservoir at the nozzle and heated to ca. 30 °C to produce formaldehyde gas. C_5F_5N was kept at room temperature in a deposit inserted in the gas line close to the vacuum chamber of the spectrometer. In the CP-FTMW instrument, which covers the 2–8 GHz frequency range, the spectra were recorded in steps of 2 GHz. The carrier gas was Ne at backing pressures of about 2 bar expanding through a 0.8 mm nozzle in pulses of 700 μs duration. Chirp pulses of 4 μs were created by an arbitrary waveform generator and amplified to 20 W. The polarization signal was radiated from a horn antenna in a direction perpendicular to that of the expanding gas. A molecular transient emission spanning 40 μs is then detected through a second horn, recorded with a digital oscilloscope and Fourier-transformed to the frequency domain. The accuracy of frequency measurements is better than 10 kHz. In the FP-FTMW instrument, operated in the 5–13 GHz frequency range, Ne was also used at stagnation pressures ranging up to 2 bar expanding in pulses of about 800 μs through a 0.8 mm nozzle. Short (typ. 0.3 μs, 10–300 mW) microwave pulses were used for polarization purposes. Typically, a ca. 400 μs-length time domain spectrum was recorded in 40–100 ns intervals and converted to the frequency domain by a fast Fourier transformation. Due to the collinear arrangement of the jet and resonator axis each rotational transition splits in two Doppler components so the resonant frequencies are taken as the arithmetic mean of both components. Frequency accuracy is better than 3 kHz. The rotational spectra of the ^{13}C and ^{15}N isotopologues in their natural abundancies were recorded in the FP-FTMW spectrometer.

Acknowledgements

JCL, AM., and SB acknowledge the Ministerio de Economía y Competitividad (Grant CTQ2016-75253-P) for financial support. A. Maris thanks the University of Bologna (RFO) and MIUR (FABR) for funding. IA thanks the Ministerio de Ciencia, Innovación y Universidades of Spain (Project No. PGC2018-094644-B-C22) and Comunidad Autónoma de Madrid (P2018/EMT-4329 AIRTEC-CM).

Conflict of Interest

The authors declare no conflict of interest.

Keywords: fluorine · molecular adducts · non-covalent interactions · pi-hole interactions · rotational spectroscopy

[1] E. A. Meyer, R. K. Castellano, F. Diederich, *Angew. Chem. Int. Ed.* **2003**, *42*, 1210–1250; *Angew. Chem.* **2003**, 115, 1244–1287.
[2] K. Müller-Dethlefs, P. Hobza, *Chem. Rev.* **2000**, *100*, 143–167.
[3] J. P. Gallivan, D. A. Dougherty, *Proc. Natl. Acad. Sci. USA* **1999**, *96*, 9459–64.
[4] M. Cametti, B. Crousse, P. Metrangolo, R. Milani, G. Resnati, *Chem. Soc. Rev.* **2012**, *41*, 31–42.
[5] R. Berger, G. Resnati, P. Metrangolo, E. Weber, J. Hulliger, *Chem. Soc. Rev.* **2011**, *40*, 3496–3508.
[6] A. Bauzá, T. J. Mooibroek, A. Frontera, *ChemPhysChem* **2015**, *16*, 2496–2517.
[7] I. Alkorta, I. Rozas, J. Elguero, *J. Org. Chem.* **1997**, *62*, 4687–4691.
[8] J. P. Gallivan, D. A. Dougherty, *Org. Lett.* **1999**, *1*, 103–105.
[9] I. Alkorta, I. Rozas, J. Elguero, *J. Am. Chem. Soc.* **2002**, *124*, 8593–8598.
[10] D. Quiñonero, C. Garau, C. Rotger, A. Frontera, P. Ballester, A. Costa, P. M. Deyà, *Angew. Chem. Int. Ed.* **2002**, *41*, 3389–3392; *Angew. Chem.* **2002**, 114, 3539–3542.
[11] A. Frontera, P. Gamez, M. Mascal, T. J. Mooibroek, J. Reedijk, *Angew. Chem. Int. Ed.* **2011**, *50*, 9564–9583; *Angew. Chem.* **2011**, 123, 9736–9756.
[12] A. Jain, V. Ramanathan, R. Sankararamakrishnan, *Protein Sci.* **2009**, *18*, 595–605.
[13] A. Jain, C. S. Purohit, S. Verma, R. Sankararamakrishnan, *J. Phys. Chem. B* **2007**, *111*, 8680–8683.
[14] T. Korenaga, H. Tanaka, T. Ema, T. Sakai, *J. Fluorine Chem.* **2003**, *122*, 201–205.
[15] J. C. Amicangelo, D. G. Irwin, C. J. Lee, N. C. Romano, N. L. Saxton, *J. Phys. Chem. A* **2013**, *117*, 1336–1350.
[16] L. Evangelisti, K. Brendel, H. Mäder, W. Caminati, S. Melandri, *Angew. Chem. Int. Ed.* **2017**, *56*, 13699–13703; *Angew. Chem.* **2017**, 129, 13887–13891.
[17] C. Calabrese, Q. Gou, A. Maris, W. Caminati, S. Melandri, *J. Phys. Chem. Lett.* **2016**, *7*, 1513–1517.
[18] W. Li, I. Usabiaga, C. Calabrese, L. Evangelisti, A. Maris, L. B. Favero, S. Melandri, *Phys. Chem. Chem. Phys.* **2021**, *23*, 9121–9129.
[19] S. Suzuki, P. G. Green, R. E. Bumgarner, S. Dasgupta, W. A. Goddard, G. A. Blake, *Science* **1992**, *257*, 942–945.
[20] P. Halder, M. S. Krishnan, E. Arunan, *J. Mol. Spectrosc.* **2020**, *370*, 111277.
[21] R. B. Mackenzie, C. T. Dewberry, R. D. Cornelius, C. J. Smith, K. R. Leopold, *J. Phys. Chem. A* **2017**, *121*, 855–860.
[22] D. A. Rodham, S. Suzuki, R. D. Suenram, F. J. Lovas, S. Dasgupta, W. A. Goddard, G. A. Blake, *Nature* **1993**, *362*, 735–737.
[23] L. Spada, N. Tasinato, F. Vazart, V. Barone, W. Caminati, C. Puzzarini, *Chem. Eur. J.* **2017**, *23*, 4876–4883.
[24] S. Blanco, J. C. López, *J. Phys. Chem. Lett.* **2018**, *9*, 4632–4637.
[25] S. Blanco, A. Macario, J. C. López, *Phys. Chem. Chem. Phys.* **2019**, *21*, 20566–20570.
[26] J.-U. Grabow, W. Caminati, *Front. Mol. Spectrosc.* **2009**, 383–454.
[27] B. H. Pate, *Science* **2011**, *333*, 947–948.
[28] W. Caminati, J.-U. Grabow, *Front. Mol. Spectrosc.* **2009**, 455–552.

[29] S. Blanco, P. Pinacho, J. C. López, *Angew. Chem. Int. Ed.* **2016**, *55*, 9331–9335; *Angew. Chem.* **2016**, 128, 9477–9481.
[30] S. Blanco, A. Macario, J. García-Calvo, A. Revilla-Cuesta, T. Torroba, J. C. López, *Chem. Eur. J.* **2021**, *27*, 1680–1687.
[31] C. Pérez, A. L. Steber, A. M. Rijs, B. Temelso, G. C. Shields, J. C. Lopez, Z. Kisiel, M. Schnell, *Phys. Chem. Chem. Phys.* **2017**, *19*, 14214–14223.
[32] P. Pracht, F. Bohle, S. Grimme, *Phys. Chem. Chem. Phys.* **2020**, *22*, 7169–7192.
[33] Gaussian 16, Revision A.03, M. J. Frisch, M. J. Trucks, H. B. Schlegel, G. E. Scuseria, M. A. Robb, J. R. Cheeseman, G. Scalmani, V. Barone, G. A. Petersson, H. Nakatsuji, X. Li, M. Caricato, A. V. Marenich, J. Bloino, B. G. Janesko, R. Gomperts, B. Mennucci, H. P. Hratchian, J. V. Ortiz, A. F. Izmaylov, J. L. Sonnenberg, D. Williams-Young, F. Ding, F. Lipparini, F. Egidi, J. Goings, B. Peng, A. Petrone, T. Henderson, D. Ranasinghe, V. G: Zakrzewski, J. Gao, N. Rega, G. Zheng, W. Liang, M. Hada, M. Ehara, K. Toyota, R. Fukuda, J. Hasegawa, M. Ishida, T. Nakajima, Y. Honda, O. Kitao, H. Nakai, T. Vreven, K. Throssell, J. A. Montgomery Jr., J. E. Peralta, F. Ogliaro, M. J. Bearpark, J. J. Heyd, E. N. Brothers, K. N. Kudin, V. N. Staroverov, T. A. Keith, R. Kobayashi, J. Normand, K. Raghavachari, A. P. Rendell, J. C. Burant, S. S. Iyengar, J. Tomasi, M. Cossi, J. M. Millam, M. Klene, C. Adamo, R. Cammi, J. W. Ochterski, R. L. Martin, K. Morokuma, O. Farkas, J. B. Foresman, D. J. Fox, Gaussian, Inc., *Wallingford CT*, **2016**.
[34] C. Møller, M. S. Plesset, *Phys. Rev.* **1934**, *46*, 618–622.
[35] M. J. Frisch, J. A. Pople, J. S. Binkley, *J. Chem. Phys.* **1984**, *80*, 3265–3269.
[36] P. J. Stephens, F. J. Devlin, C. F. Chabalowski, M. J. Frisch, *J. Phys. Chem.* **1994**, *98*, 11623–11627.
[37] S. Grimme, J. Antony, S. Ehrlich, H. Krieg, *J. Chem. Phys.* **2010**, *132*, 154104.
[38] S. Grimme, S. Ehrlich, L. Goerigk, *J. Comput. Chem.* **2011**, *32*, 1456–1465.
[39] R. A. Kendall, T. H. Dunning, R. J. Harrison, *J. Chem. Phys.* **1992**, *96*, 6796–6806.
[40] G. E. Scuseria, C. L. Janssen, H. F. Schaefer, *J. Chem. Phys.* **1988**, *89*, 7382–7387.
[41] G. G. Brown, B. C. Dian, K. O. Douglass, S. M. Geyer, S. T. Shipman, B. H. Pate, *Rev. Sci. Instrum.* **2008**, *79*, 4–5.
[42] P. Pinacho, S. Blanco, J. C. López, *Phys. Chem. Chem. Phys.* **2019**, *21*, 2177–2185.
[43] T. J. Balle, W. H. Flygare, *Rev. Sci. Instrum.* **1981**, *52*, 33–45.
[44] J. U. Grabow, W. Stahl, H. Dreizler, *Rev. Sci. Instrum.* **1996**, *67*, 4072–4084.
[45] D. R. Johnson, F. J. Lovas, W. H. Kirchhoff, *J. Phys. Chem. Ref. Data* **1972**, *1*, 1011–1046.
[46] S. Doraiswamy, S. D. Sharma, *Chem. Phys.* **1974**, *6*, 76–86.
[47] H. M. Pickett, *J. Mol. Spectrosc.* **1991**, *148*, 371–377.
[48] W. Gordy, R. L. Cook, *Microwave Molecular Spectra*, Wiley-Interscience, New York, **1984**.
[49] J. K. G. Watson, in *Vib. Spectra Struct. a Ser. Adv. Vol 6* (Ed.: J. R. Durig), Elsevier, New York, **1977**, pp. 1–89.
[50] J. Kraitchman, *Am. J. Phys.* **1953**, *21*, 17–24.
[51] Z. Kisiel, *J. Mol. Spectrosc.* **2003**, *218*, 58–67.
[52] R. Meyer, *J. Mol. Spectrosc.* **1979**, *76*, 266–300.
[53] R. F. W. Bader, *Chem. Rev.* **1991**, *91*, 893–928.
[54] J. Contreras-García, E. R. Johnson, S. Keinan, R. Chaudret, J. P. Piquemal, D. N. Beratan, W. Yang, *J. Chem. Theory Comput.* **2011**, *7*, 625–632.
[55] G. Jansen, A. Hesselmann, H. L. Williams, C. F. Chabalowski, *J. Phys. Chem. A* **2001**, *105*, 11156–11158.
[56] A. Hesselmann, *J. Chem. Theory Comput.* **2018**, *14*, 1943–1959.
[57] M. O. Sinnokrot, E. F. Valeev, C. D. Sherrill, *J. Am. Chem. Soc.* **2002**, *124*, 10887–10893.
[58] J. Alonso, F. J. Lorenzo, J. C. López, A. Lesarri, S. Mata, H. Dreizler, *Chem. Phys.* **1997**, *218*, 267–275.

Manuscript received: June 18, 2021
Accepted manuscript online: August 4, 2021
Version of record online: September 2, 2021

